

A mean density of $112 M_{\odot} \text{pc}^{-3}$ for Central Molecular Zone clumps – Evidences for shear-enabled pressure equilibrium in the Galactic Center

GUANG-XING LI¹ AND CHUAN-PENG ZHANG^{2,3}

¹*South-Western Institute for Astronomy Research, Yunnan University,
Kunming, 650500 Yunnan, P.R. China*

²*National Astronomical Observatories, Chinese Academy of Sciences, 100101 Beijing, P.R. China*

³*CAS Key Laboratory of FAST, National Astronomical Observatories, Chinese Academy of Sciences, 100101 Beijing, P.R. China*

(Received June 1, 2019; Revised January 10, 2019; Accepted February 1, 2022)

Submitted to APJ

ABSTRACT

We carry out a systematic study of the density structure of gas in the Central Molecular Zone (CMZ) in the Galactic center by extracting clumps from the APEX Telescope Large Area Survey of the Galaxy survey at $870 \mu\text{m}$. We find that the clumps follow a scaling of $m = \rho_0 r^3$ which corresponds to a characteristic density of $n_{\text{H}_2} = 1.6 \times 10^3 \text{cm}^{-3}$ ($\rho_0 = 112 M_{\odot} \text{pc}^{-3}$) with a variation of ≈ 0.5 dex, where we assumed a gas-to-dust mass ratio of 100. This characteristic density can be interpreted as the result of thermal pressure equilibrium between the molecular gas and the warm ambient interstellar medium. Such an equilibrium can plausibly be established since shear has approximately the same strength as self-gravity. Our findings may explain the fact that star formation in the CMZ is highly inefficient compared to the rest of the Milky Way disk. We also identify a population of clumps whose densities are two orders of magnitudes higher in the vicinity of the Sgr B2 region, which we propose are produced by collisions between the clumps of lower densities. For these collisions to occur, processes such as compressive tides probably have created the appropriate condition by assembling the clumps together.

Keywords: Galactic center (565); Interstellar medium (847); Star formation (1569); Tidal interaction (1699); Gravitational collapse (662);

1. INTRODUCTION

The Central Molecular Zone (CMZ) is a disk-like gas structure that rotates around the center of the galaxy. The region has a size of $\approx 500 \text{pc}$, and it contains a total of $3 \times 10^7 M_{\odot}$ of molecular gas (Bally et al. 1987; Dahmen et al. 1998). The gas rotates at a speed of $\approx 200 \text{km s}^{-1}$ where the centrifugal force is likely to be balanced by gravity from the central stellar bulge (Sofue 2013)¹. Different from “ordinary” molecular clouds (e.g. Heyer & Dame 2015), gas in the CMZ is characterized by a higher degree of turbulent motion (Shetty et al. 2012).

It has been found that the star formation of dense gas in the CMZ is one order of magnitude lower compared to that of the Milky Way (Longmore et al. 2013; Kruijssen et al. 2014; Barnes et al. 2017; Kauffmann et al. 2017a).

Studying the evolution of gas in the CMZ is important for two reasons: first, the fact that the gas dynamics and star formation in the CMZ are distinct from the rest of the Milky Way means CMZ is a unique laboratory where we can deepen our understanding of the star formation process. Second, understanding the evolution of gas in the CMZ is a key to understanding gas transport between the Galactic disk and the central black hole, and can provide insights into other important questions such as black hole growth, Active Galactic Nucleus (AGN) feedback, and galactic disk evolution.

A very first step toward understanding the gas evolution is to study the density structure, which we focus

Corresponding author: Guang-Xing Li, Chuang-Peng Zhang
gxli@ynu.edu.cn, cpzhang@nao.cas.cn

¹ The exact geometry of the region is still under debate (Churazov et al. 2017).

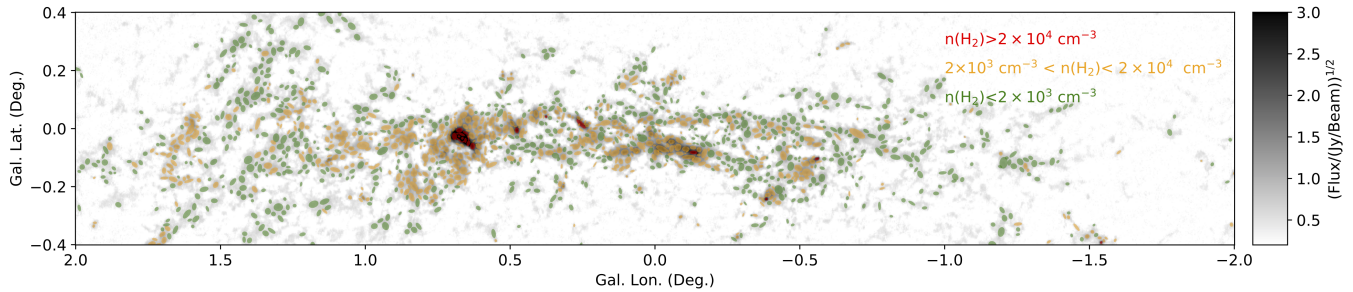


Figure 1. Spatial distribution of clumps of different densities. The grayscale image in the background is the $870\ \mu\text{m}$ continuum emission map from the ATLASGAL survey (Schuller et al. 2009). Overlaid ellipses in different colors represent clumps of different densities extracted using the GAUSSCLUMPS algorithm. The densities are indicated at the upper right of the panel.

on in this paper. There have been plenty of studies that characterize the (spatial, kinematic, and chemical) structure of molecular gas in the CMZ (e.g. Jones et al. 2008; Bally et al. 2010; Kruijssen et al. 2015; Henshaw et al. 2016). However, a detailed study on the density structure of the CMZ and its evolution down to sub-pc scale is still lacking.

In this paper, we study the density structure of the CMZ region using data from the APEX Telescope Large Area Survey of the Galaxy (ATLASGAL; Schuller et al. 2009). ATLASGAL is a survey of the inner Galaxy at $870\ \mu\text{m}$ performed by the APEX telescope (Güsten et al. 2006). It has a spatial resolution of around $19''$. Continuum observations at $870\ \mu\text{m}$ atmospheric window are well-suited for tracing the cold gas. Besides, the $19''$ resolution translates to a scale of 0.8 pc assuming that we are $\approx 8.2\text{ kpc}$ (Gravity Collaboration et al. 2019) away from the CMZ, guaranteeing that the majority of the dense clumps at the CMZ region are reasonably resolved. Compared to previous surveys such as the BGPS (Bolocam Galactic Plane Survey) (Aguirre et al. 2011), the ATLASGAL survey has a much higher detection sensitivity ($\sigma = 0.05\text{ Jy beam}^{-1}$). Taking advantage of this, we perform a systematic study of the structure of gas in the whole CMZ region, and perform a joint analysis of the statistical properties of the gas clumps with their positions and discuss the implications.

2. OBSERVATIONS AND ANALYSIS

2.1. Continuum data at $870\ \mu\text{m}$

We use $870\ \mu\text{m}$ continuum map from ATLASGAL² survey (Schuller et al. 2009) to study the density structure of dense gas in the CMZ. The ATLASGAL data³

are well-suited to the study of small-scale ($0.8\text{--}6\text{ pc}$), high surface density structures (structures whose surface densities are larger than $140\ M_{\odot}\text{ pc}^{-2}$). On the smaller side, we are limited by our resolution, which is 0.8 pc . On the larger side, structures of large sizes (larger than 2.5 , or 6 pc) are filtered out due to the limitation of ground-based bolometer observations (Schuller et al. 2009). Structures with surface densities lower than $140\ M_{\odot}\text{ pc}^{-2}$ can not be reliably detected due to our limited sensitivity ($\sigma = 0.05\text{ Jy beam}^{-1}$). Due to the limited spatial dynamical range, we might underestimate the mass of the larges clumps by up to 50% (Mattern et al. 2018).

2.2. Clump extraction

To capture the density structure of the molecular gas and study its spatial variations, we use the algorithm GAUSSCLUMPS (Stutzki & Güsten 1990; Kramer et al. 1998) in the GILDAS⁴ software package to extract dense clumps. This method has been successfully adopted in Zhang et al. (2018, 2019). We extract clumps by fitting Gaussians to a well-resolved peaks whose intensities $I_{870\ \mu\text{m}}$ are above 5σ ($\sigma = 0.05\text{ Jy beam}^{-1}$) and whose FWHMs are larger than $19''$ ($870\ \mu\text{m}$ beam size). The 1483 identified clumps are plotted in Figure 1, and the physical parameters are listed in Table 1.

2.3. Dust temperature estimation

To accurately derive the clump mass it is necessary to estimate the dust temperature. Using high-quality Hi-GAL (Herschel infrared Galactic Plane Survey) data covering a large wavelength ranging from 70 to $500\ \mu\text{m}$ (Molinari et al. 2016),⁵ we calculate the dust temperature map via fitting the spectral energy distribution (SED) extracted from the multiwavelength images on a

² The ATLASGAL project is a collaboration between the Max-Planck-Gesellschaft, the European Southern Observatory (ESO), and the Universidad de Chile.

³ Available at https://atlasgal.mpifr-bonn.mpg.de/cgi-bin/ATLASGAL_DATABASE.cgi.

⁴ <https://www.iram.fr/IRAMFR/GILDAS/>

⁵ Available at <https://irsa.ipac.caltech.edu/applications/Herschel/>.

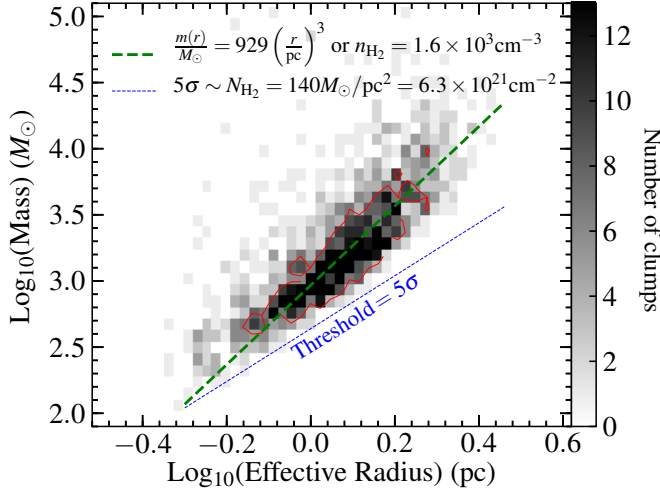


Figure 2. Mass–size distribution of the clumps with a threshold $I_{870\mu\text{m}} > 5\sigma$ (indicated by blue dotted line) in the CMZ region. The green dashed line stands for $m_{\text{clump}}/M_{\odot} = 929 (r/\text{pc})^3$, which corresponds to $n_{\text{H}_2} = 1.6 \times 10^3 \text{ cm}^{-3}$. Note that to compute the volume density, we have used Eq. 5, whose justification can be found in Appendix B. The red contour represents locations with more than seven clumps per pixel. See Sec. 2.4 for details.

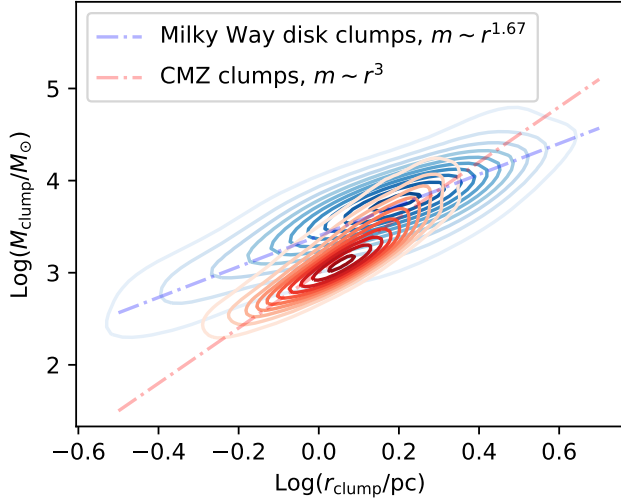


Figure 3. Clumps–scale mass–size relation. The blue contours represent the distribution of proto–cluster clumps in the mass–size plane. The data come from (Urquhart et al. 2013). The blue line represents the scaling $m_{\text{clump}} \propto r_{\text{clump}}^{1.67}$ proposed in (Li 2017a). The red contours represent the distribution of CMZ clumps in the mass–size plane, and the red line represents the scaling $m_{\text{clump}} \propto r_{\text{clump}}^3$ found in this work. The contours are constructed using density fields estimated from the KDE (kernel density estimation) algorithm.

pixel-by-pixel basis (e.g. Wang et al. 2015). This method has been successfully adopted in many works, such as Zhang et al. (2017a,b) and Zhou et al. (2019). In our calculations, a smooth component is removed using a Fourier transform-based approach (Wang et al. 2015). In this method, the original images have been transformed into the Fourier domain and separated into the low and high spatial frequency components, and then inversely transferred back into the image domain. The low-frequency component corresponds to large-scale background/foreground emission, while the high-frequency component represents the emission of interest. In spite of this, we might still be contaminated by clumps in the Milky Way disks. However, these clumps are small in number (10 %, estimated from Csengeri et al. 2014) and do not contribute significantly to our statistics. In current work, we regridded the maps to the same resolution of $11''.5$, and convolved the images with the same Gaussian beam with $\text{FWHM} = 45''$, corresponding to the measured beam size of $500 \mu\text{m}$ data. Other parameter setup is the same as that in Zhang et al. (2017a). The dust temperature T_{dust} map was shown in Appendix A.

2.4. Mass and density calculation

Assuming that the dust emission is optically thin, we calculate the clump masses M_{H_2} following Kauffmann et al. (2008) via

$$\left(\frac{M_{\text{H}_2}}{M_{\odot}}\right) = 0.12 \left(e^{14.39 \left(\frac{\lambda}{\text{mm}}\right)^{-1} \left(\frac{T_{\text{dust}}}{\text{K}}\right)^{-1}} - 1 \right) \times \left(\frac{\kappa_{\nu}}{\text{cm}^2 \text{g}^{-1}} \right)^{-1} \left(\frac{S_{\nu}}{\text{Jy}} \right) \left(\frac{D}{\text{kpc}} \right)^2 \left(\frac{\lambda}{\text{mm}} \right)^3 \left(\frac{\eta_{\text{gas}}}{100} \right) \quad (1)$$

where $\lambda = 870 \mu\text{m}$ is the observational wavelength, T_{dust} is the dust temperature (see Section 2.3), $\kappa_{\nu} = 0.0185 \text{ cm}^2 \text{g}^{-1}$ is the dust opacity at $870 \mu\text{m}$ (Ossenkopf & Henning 1994), D is the distance to the Sun, η_{gas} is the gas-to-dust ratio and integrated flux S_{ν} is

$$S_{\nu} = I_{\text{peak}} \times \frac{\text{FWHM}_{\text{ext}}^2}{\text{FWHM}_{\text{obs}}^2}, \quad (2)$$

where FWHM_{ext} is the extracted Gaussian size of each clump by GAUSSCLUMPS, and FWHM_{obs} is the beam size of the ATLASGAL observations. We assume that all the clumps we analyze sit at a distance of 8.2 kpc (Gravity Collaboration et al. 2019).

The surface density of the clumps are estimated as

$$\Sigma_{\text{clump}} = m_{\text{clump}} / \pi r_{\text{clump}}^2, \quad (3)$$

where r_{eff} is related to FWHM by $r_{\text{eff}} = \text{FWHM} / (2\sqrt{\ln 2})$. The H_2 column density is related

to the surface density by

$$N(\text{H}_2) = \Sigma_{\text{H}_2} / (\mu_{\text{H}_2} m_{\text{H}}), \quad (4)$$

where $\mu_{\text{H}_2} \approx 2.8$ is the mean molecular weight (e.g. [Kauffmann et al. 2008](#)).

If the cores are considered as uniform spheres, the volume density n_{H_2} can be estimated by

$$\rho_{\text{clump}} = 0.12 m_{\text{clump}} / r_{\text{eff}}^3, \quad (5)$$

a detailed justification of this formula can be found in Appendix B. For convenience, we also express the gas density in terms of the number of H_2 molecules found per cubic centimeter, where

$$n_{\text{H}_2} = \frac{\rho_{\text{clump}}}{\mu_{\text{H}_2} m_{\text{H}}}, \quad (6)$$

The derived parameters are listed in Table 1.

In our fiducial calculations, we make the working assumption that the gas-to-dust mass ratio η_{gas} is 100, which is essentially the value reported in the solar neighborhood. We have adopted this assumption to ensure that the values we derived are comparable to the values reported from the other authors. Nevertheless, this assumption is unlikely to be accurate, as the gas-to-dust ratio is expected to evolve significantly with respect to metallicity and hence Galactocentric distance. By extrapolating results from [Giannetti et al. \(2017\)](#), the gas-to-dust ratio in the Galactic center might be lower than 50. This uncertainty must be kept in mind when interpreting the results.

3. RESULTS

3.1. Mass, Size and density distributions

We study the density distribution of gas on scales from 0.8 to 6 pc and column density $\gtrsim 140 M_{\odot} \text{ pc}^{-2}$, which can be reliably recovered by the ATLASGAL survey. Figure 1 plots the results of our clump extraction obtained using the GAUSSCLUMPS, where each clump is represented with an ellipse. Our source extraction has captured the majority significant structures ($I_{870\mu\text{m}} > 5\sigma$) visible on the map. In total, we have recovered a mass of $5.38 \pm 0.05 \times 10^6 M_{\odot}$, which is much larger than the mass of $6 \times 10^5 M_{\odot}$ recovered by the BGPS survey ([Bally et al. 2010](#)). However, our total mass is still smaller than that ($\approx 3 \times 10^7 M_{\odot}$) reported in [Bally et al. \(1987\)](#) and [Dahmen et al. \(1998\)](#) estimated using CO observations of a much lower resolution. This difference is caused by a combination of: (1) they analyzed an area that is twice as large as ours, and (2) although our observations have significantly better angular resolutions, we are more limited in sensitivity and spatial dynamical range. The ^{13}CO observations of [Bally et al. \(1987\)](#)

allow them to probe gas with much lower surface densities (e.g. a few tens of $M_{\odot} \text{ pc}^{-2}$), which is around 1 order of magnitude lower than our limiting surface density. Presumably, there are gases whose surface densities lie between 50 to $140 M_{\odot} \text{ pc}^{-2}$. These gases can be detected (yet unresolved) in [Bally et al. \(1987\)](#) but remain undetected by ATLASGAL.

Figure 2 plots the distribution of clumps in the mass-size plane. This distribution is clearly different from that of the “ordianry” ATLASGAL clumps (Figure 3). Above the detection limit, the clumps have a structured distribution, where pixels that contain the largest number of clumps seem to follow a relation with $m_{\text{clump}} \propto r_{\text{clump}}^3$, which points to a constant density that is independent on the scale. We note that this characteristic density is somehow dependent on whether we weight the density distribution by volume or by mass.

To further study the density structure of the region, in Figure 4, we plot both the volume-weighted and mass-weighted density distribution of the clumps. From the volume-weighted plot, we measure a characteristic density of $n_{\text{H}_2} = 1.6 \times 10^3 \text{ cm}^{-3}$, $\rho_0 = 112 M_{\odot} \text{ pc}^{-3}$ by fitting a log-normal function to the distribution and a density variation of ≈ 0.5 dex is measured from the FWHM of the distribution. This corresponds to a mass-size relation of

$$m_{\text{clump}} / M_{\odot} = 929 (\eta_{\text{gas}} / 100) (r / \text{pc})^3, \quad (7)$$

where the density and the normalization of the mass-size relation is related by Eq. 5.

To further demonstrate the existence of this characteristic density, in the right panel of Fig. 4, we plot the mass-weighted density distribution of groups of clumps of different sizes. Since the peaks of the density distributions from these subsamples do not evolve with the clump radii, the characteristic density that we derived is an intrinsic property shared by these clumps.

3.2. Spatial distribution of clumps of different densities

Although our clumps sample exhibits a density variance of ≈ 0.5 dex, a significant number of clumps have densities that are two orders of magnitudes larger than the mean density. To better understand the density structure of the region, in Figure 4, we divide the clumps into three groups: the first group of clumps has a density of $n_{\text{H}_2} < 2.0 \times 10^3 \text{ cm}^{-3}$, which is called “lower-density clumps”, the second group of clumps has a density of $2.0 \times 10^4 > n_{\text{H}_2} > 2.0 \times 10^3 \text{ cm}^{-3}$, which we call “higher-density clumps”, and the third group of clumps has a density of $n_{\text{H}_2} \gtrsim 2.0 \times 10^4 \text{ cm}^{-3}$, which is called as “highest-density clumps”. The “highest-density clumps” seems to belong to a parameter range

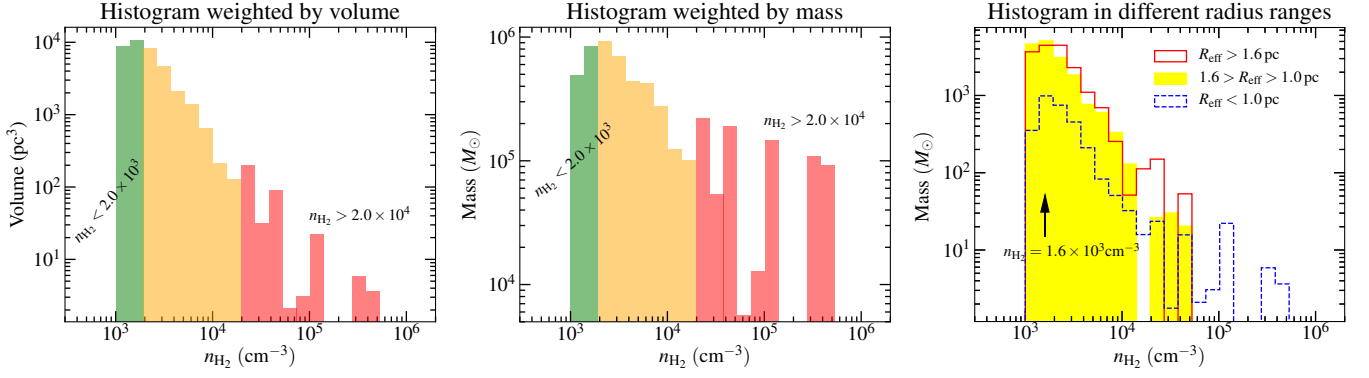


Figure 4. Density distribution of the CMZ region. Left panel: Volume-weighted density histogram of the CMZ region. Middle panel: Mass-weighted density histogram of the CMZ region. In these panels, contributions from clumps of different densities are indicated with different colors. Right panel: Volume-weighted density histogram of clumps of different sizes. Clumps of different sizes seem to share a common mean density of $n_{\text{H}_2} = 1.6 \times 10^3 \text{ cm}^{-3}$.

that is separated from the majority of the clumps indicated by the discontinuity of density distribution in Figure 4.

We then plot the spatial distributions of clumps of different densities in Figure 1. It emerges that the spatial distribution of the higher-density clumps exhibits a pattern where they seem to follow an arc-like structure which stretches from $l = 1^\circ$ to $l = -1^\circ$, and it contains some of the most active star-forming regions in the CMZ like the Sgr B2. To some extent, one can relate our dense arc to the 100-pc twisted ring identified by Molinari et al. (2011), where dense gas (gas with densities above $n_{\text{H}_2} \approx 2.0 \times 10^3 \text{ cm}^{-3}$) forms a coherent, twisted pattern, and we note that in addition to that, gas is unevenly distributed along this ring, with clumps of the highest densities ($n_{\text{H}_2} \gtrsim 2.0 \times 10^4 \text{ cm}^{-3}$) distribute mostly within the vicinity of the Sgr B2 region. This uneven distribution of dense gas implies that the dynamics of the region are non-stationary, as expected from some recent models (e.g. Kruijssen et al. 2015; Henshaw et al. 2016; Sormani et al. 2018).

4. DISCUSSIONS

4.1. Mass-size relation as density structure diagnostics

We focus on the mass-size relation of clump-scale dense gas revealed by the ATLASGAL survey. Our mass-size relation should be distinguished from the core-scale mass-size relation seen in (e.g. Lada et al. 2008), and various cloud-scale mass-size relation (e.g. Roman-Duval et al. 2010) summarized in Chen et al. (2020). We remind the reader that we use ATLASGAL observations at $870\mu\text{m}$ obtained with the APEX telescope. Due to the fact that the emission from dust is optically thin, the ATLASGAL survey data is ideal for tracing the distribution of dense gas in the Milky Way (where

$\Sigma_{\text{gas}} \geq 140 M_\odot \text{ pc}^{-2}$). In the Milky Way disk, all the dense clumps seen in ATLASGAL should collapse to form star clusters in a few crossing time (Wyrowski et al. 2012, 2016; Li 2018) whereas in the Milky Way center they do not appear to be collapsing.

On the clump scale, structures in the Milky Way disk follow $m \propto r^{1.67}$ (e.g. Urquhart et al. 2013; Pfalzner et al. 2016; Li 2017a), meaning that larger clumps have smaller densities. In contrast to this, in the Galactic center, the clumps seem to have a density that is independent on the clump size. This reflects the uniqueness of the CMZ in terms of density structure. A comparison is made in Fig. 3.

4.1.1. Evidence of pressure equilibrium

We propose that this almost-constant gas density observed in the CMZ region can be explained by the thermal pressure equilibrium. The gas temperature is found to be around 50 – 100 K (Nagai et al. 2007; Ao et al. 2013; Ginsburg et al. 2016). Assuming a temperature of 70 K, we estimate that the cold gas has a pressure of

$$\frac{p_{\text{internal}}}{k_B} = n_{\text{H}_2} T_{\text{gas}} (\eta_{\text{gas}}/100) \approx 1.1 \times 10^5 \text{ K cm}^{-3}, \quad (8)$$

where we assumed $n_{\text{H}_2} = 1.6 \times 10^3 \text{ cm}^{-3}$, k_B is the Boltzmann constant.

As a comparison, using temperature measured by Yamauchi et al. (1990), Spergel & Blitz (1992) estimated a pressure of

$$p_{\text{external}}/k_B \approx 10^5 - 10^6 \text{ K cm}^{-3}, \quad (9)$$

for the warm ambient gas, where the pressure is computed using $p = nk_B T$. The temperature and density can be estimated by modeling the X-ray emission, and the pressure we estimated is broadly consistent with results reported in the literature (e.g. Munro et al. 2004;

Ponti et al. 2015, 2019; Nakashima et al. 2019). Since $p_{\text{internal}} \approx p_{\text{external}}$, thermal pressure equilibrium does provide a good explanation to the observed gas density.

We still observe a density fluctuation of around 0.5 dex, which can be caused by processes such as turbulence. Turbulence is known to be capable of producing density variations (Vazquez-Semadeni 1994; Padoan et al. 1997; Scalo et al. 1998; Federrath et al. 2010). The clumps we observed have a (volume-weighted) density variation of ≈ 0.5 dex. Adopting the relation between density variation and Mach number from Konstandin et al. (2012), this can be produced by turbulence with a Mach number of around 2. This requires a turbulent velocity dispersion of a few km s^{-1} for solenoidal turbulence, where we adopt an isothermal sound speed of around 0.5 km s^{-1} (the sound speed is derived assuming a temperature of 70 K). This is smaller yet comparable to the typical clump-scale velocity dispersion found in Shetty et al. (2012) measured at a scale of around 1 pc. Turbulence is capable of producing the observed density variations.

Finally, we note that in our picture, an equilibrium is established between the thermal pressure of cold gas in the clump and the thermal pressure of the ambient hot gas, and turbulence can only create additional density variations. Our view is shared by Wolfire et al. (2003).

4.1.2. Regulation of collapse by shear

Even in the Milky Way disk, thermal pressure equilibrium does play an important role in setting the density of the molecular gas (Spitzer & Tomasko 1968; Field et al. 1969), however, clumps in the Galactic disks are dense objects that sit at the centers of molecular clouds, and their densities are mainly determined by an interplay between turbulence and gravity (Li 2017a). In contrast, the clumps in the CMZ share a density that is mostly independent of the clump radius. We propose that this can be explained in a *shear-enabled pressure equilibrium* scenario where shear is able to counteract against gravitational collapse.

In the absence of shear, self-gravity is dynamically important for these clumps. We first estimate the effective pressure caused by gravity, which is

$$\begin{aligned} \frac{p_{\text{gravity}}}{k_B} &\approx \frac{Gm_{\text{clump}}^2}{k_B r^2} \times \frac{1}{4\pi r^2} \approx \frac{G\pi\Sigma_{\text{clump}}^2}{4k_B} \approx \frac{9G\pi\rho^2 r_{\text{clump}}^2}{4k_B} \\ &\approx 2 \times 10^6 \text{ K cm}^{-3} \left(\frac{r_{\text{clump}}}{\text{pc}} \right)^2 \left(\frac{\eta_{\text{gas}}}{100} \right)^2, \end{aligned} \quad (10)$$

where r_{clump} is the size of a clump, and we have assumed $\Sigma_{\text{clump}} = m_{\text{clump}}/(\pi r_{\text{clump}}^2)$, $\Sigma_{\text{clump}} \approx 3\rho_{\text{clump}} r_{\text{clump}}$ ⁶,

⁶ Derived by combining Eq. 3 and Eq. 5.

and $\rho_{\text{clump}} = 112M_{\odot} \text{ pc}^{-3}$. For a typical clump of size $\approx 1 \text{ pc}$, this pressure is indeed comparable to the internal and external pressure we estimated before, and one would naively expect gravity to be able to compress the gas significantly.

Although gravity should be a major player, in the CMZ, its effect is largely canceled by effects like shear and extensive tidal force. Shear can cause gas at different radii to rotate at different angular speeds, and this differential motion stretches gas into long streams before they can collapse on their own. Tidal force causes different parts of a clump to accelerate differently, and it can halt the fragmentation when the tidal force is extensive.

The fact that gas clumps organize into streams (e.g. Henshaw et al. 2016) indicates that shear should be dynamically important. To evaluate the relative importance between shear and self-gravity, we compute the relevant timescales. Assuming that the rotation curve of the CMZ gas can be parameterized as $v \propto r^p$, the shear time is

$$\begin{aligned} t_{\text{shear}} &= \left(\frac{\partial\Omega}{\partial r} r \right)^{-1} = \left| \frac{1}{1-p} \right| \Omega^{-1} \\ &\approx 1.1 \times \Omega^{-1} \approx 1.7 |1-p|^{-1} \text{ Myr} \\ &\approx 2.8 \text{ Myr}, \end{aligned} \quad (11)$$

where we have assumed $p \approx 0.4$. To estimate the value of p , we use the mass profile derived by Kruijssen et al. (2015), which is based on the mass profile of Launhardt et al. (2002).

For comparison, the time for gravitational collapse to occur on a sphere of a constant density is

$$\begin{aligned} t_{\text{ff}} &= \sqrt{\frac{3\pi}{32G\rho_{\text{gas}}}} \\ &\approx 0.54 \times \sqrt{\frac{1}{G\rho_{\text{gas}}}} \approx 0.7(\eta_{\text{gas}}/100)^{-1/2} \text{ Myr} \end{aligned} \quad (12)$$

where we have used $\rho_{\text{gas}} = 112M_{\odot} \text{ pc}^{-2}$, where η_{gas} is the gas-to-dust mass ratio, and its value is still uncertain and can range from 10 to 100. To interpret these numbers, we note that both the shear time and the freefall time are subject to significant uncertainties. The shear time is sensitive to the shape of the rotation profile measured in terms of p in Eq. 11. The version of the rotation profile used in this paper is derived using the stellar mass model presented in Launhardt et al. (2002) and a discussion on its uncertainty seems to be missing. The freefall time, which is dependent on the gas density and hence the gas-to-dust ratio, is also uncertain (Sec. 2.4). Assuming that $p = 1$ and $\eta_{\text{gas}} = 100$,

the shear time is around 3 Myr, which appears to be ≈ 4 times the freefall time. However, since recent observations seem to indicate that the η_{gas} can be as low as 10 in the Galactic center, it seems plausible that the shear time is comparable to the freefall time. The current data is consistent with the proposal that shear can counteract against gravitational collapse in the Galactic center region.

Our findings provide crucial insights into the puzzle of the inefficiency of star formation in the CMZ region. It is believed that enhanced turbulence is responsible for the inefficiency of star formation (Kruijssen et al. 2014). Here, our analyses have revealed that in the CMZ region, shear has the adequate strength to halt the collapse of the individual clumps. Our results agree with earlier proposals that shear can be a factor to regulate collapse in the CMZ region (e.g. Launhardt et al. 2002; Longmore et al. 2013; Emsellem et al. 2015; Krumholz & Kruijssen 2015; Jeffreson et al. 2018), although in those papers shear is expected to halt the collapse of the CMZ on the large scale, preventing it to collapse globally, whereas in our case, the importance of shear is more pronounced where it can stop the collapse of the individual clumps, although other processes such as turbulence can also be important.

4.2. Forming dense gas through clump collisions

Although the densest clumps ($n_{\text{H}_2} \gtrsim 2.0 \times 10^4 \text{ cm}^{-3}$) only contains a small fraction of the mass, they are associated with the majority of star formation found in this region (see, e.g., the star formation rate of individual clouds from Kauffmann et al. 2017b). Interestingly, they are distributed almost exclusively in the vicinity of the Sgr B2 region (Figure 1).

We propose that a preferred way to produce these dense clumps is through clump collisions. It is believed that collision between molecular clouds should occur regularly in the Milky Way disk (Tasker & Tan 2009; Torii et al. 2011; Fukui et al. 2014; Gong et al. 2017). Dobbs et al. (2011) and Li (2017b) estimated the timescale for such processes to occur and found that the collision time is comparable to the dynamical time in the bulk of the Milky Way disk. In the CMZ region, the collisions can produce the dense clumps since (a) clump collisions should occur in this region regularly, and (b) these collisions are capable of producing clumps of such high densities.

To evaluate whether cloud–cloud collisions should occur near Sgr B2, the mean free path can be estimated as (Li 2017b)

$$\lambda_{\text{clump}} \approx \frac{\Sigma_{\text{clump}}}{\rho_{\text{mean}}} = \frac{100 M_{\odot} \text{ pc}^{-2}}{1000 M_{\odot} \text{ pc}^{-3}} \approx 0.1 \text{ pc}, \quad (13)$$

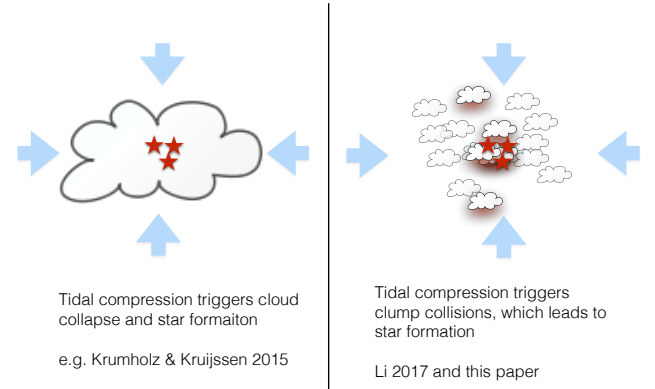


Figure 5. Different views on the origin of dense gas near Sgr B2. In previous models (Krumholz & Kruijssen 2015; Jeffreson et al. 2018; Dale et al. 2019; Kruijssen et al. 2019), it is believed that tidal force can compress gas clouds which leads the formation of dense gas and stars. In this paper (following Li 2017b), a tidal force can compress an ensemble of clumps, which triggers collisions that lead to the formation of clumps of much higher densities.

where, to estimate the mean surface density of the clumps, we have adopted a mean density of $n_{\text{H}_2} = 2 \times 10^3 \text{ cm}^{-3}$ and a typical size of 1 pc (see Figure 1), such that $\Sigma_{\text{clump}} = 100 M_{\odot} \text{ pc}^{-2}$ and the Sgr B2 region is estimated to have a mean density of $\approx 1000 M_{\odot} \text{ pc}^{-3}$ (e.g. Schmiedeke et al. 2016). The mean free path of clumps in the region is around 0.12 pc, which is much smaller than the size of the region. If the clumps in the CMZ are not collapsing by themselves, when assembled to a very small region, collisions must occur.

Can clump collisions produce these highest-density clumps? In the vicinity of the Sgr B2, the density enhancement due to collisions can be estimated as $\rho'/\rho \approx \mathcal{M}^2 = (v_{\text{collide}}/c_s)^2$ where ρ'/ρ is the density contrast. To produce a density enhancement of 100, one needs the clumps to collide at Mach number $\mathcal{M} = 10$. Assuming a sound speed of 0.5 km s^{-1} , the cloud must collide with a relative speed of a few km/s, which is possible since an inter-clump velocity dispersion of a few tens of km s^{-1} is common at the CMZ region (Henshaw et al. 2016). Our mechanism of producing dense clumps through collisions is consistent with the observational result of Tsuboi et al. (2015) where they found enhancements of SiO emission lines in the vicinity of the Sgr B2 complex, which they interpreted as the result of shocks produced during collisions.

Recent papers have pointed out that the importance of processes such as changes of shear in triggering star formation (Krumholz & Kruijssen 2015; Jeffreson et al. 2018; Dale et al. 2019; Kruijssen et al. 2019). However, the picture we are proposing is very different. In models such as Dale et al. (2019), when a cloud passes through

certain locations, tidal compression is imposed on the cloud as a whole which causes it to collapse, whereas in our case (similar to Li 2017b), an external compression cause ensembles of clumps to collide and agglomerate, through which dense gas is produced and star formation is triggered. The collisions also lead to the formation of clumps of higher masses. The different scenarios are illustrated in Figure 5.

5. CONCLUSION

Using data from the ATLASGAL survey, we study the density structure of the molecular gas in the CMZ region traced by dust continuum emission. We have extracted 1483 clumps from the data, and have studied the properties of the clumps in terms of mass, size, and density. We find that the majority of the clumps follow $m \propto r^3$, which points to a constant density of $n_{\text{H}_2} = 1.6 \times 10^3 \text{ cm}^{-3}$ ($\rho_0 = 112 \text{ M}_\odot \text{ pc}^{-3}$) where we have assumed a dust-to-gas ratio of 100. Clumps in localized regions such as the Sgr B2 vicinity have densities that are two orders of magnitudes higher than the mean density of gas in the CMZ.

We propose that this characteristic density can be explained by a *shear-enabled pressure equilibrium* model where the density is set by balance between the thermal pressure cold gas and that of the warm ambient medium. Different from “ordinary” clouds in the Milky Way disk, in the CMZ, a thermal pressure equilibrium can be achieved since shear (and possibly extensive tidal force) caused by gravity from the Galactic Bulge is strong enough to counteract against self-gravity.

Our shear-enabled pressure equilibrium scenario can explain the inefficiency of star formation of the CMZ, as shear has the adequate strength to counteract against gravitational collapse, and this mechanism is expected to reduce the star formation significantly. Although other regulating mechanisms, such as turbulence might still be playing important roles, the fact that the clumps in the CMZ follow a relation with $m_{\text{clump}} \propto r_{\text{clump}}^3$ seems to indicate that the role of shear is indispensable.

We also identified an over-abundance of clumps with $n_{\text{H}_2} > 2.0 \times 10^4 \text{ cm}^{-3}$ in the vicinity of the Sgr B2 region. We propose that they are produced by agglomerations/collisions of clumps of lower densities. For collisions to occur, processes such as tidal compression have probably provided the appropriate condition by assembling the clumps together.

Our analyses reveal that the gas in the CMZ belongs to a unique regime where shear is sufficient to overcome gravity in the individual clumps, such that the density of these clumps is determined directly by the thermal pressure equilibrium established with respect to the ambient environment. Our picture is crucial for understanding the evolution of gas at centers of other galaxies where star formation appears to be suppressed.

ACKNOWLEDGEMENTS

This work is partly supported by the National Natural Science Foundation of China 11703040. We thank Dr. Jinghua Yuan for the data reduction of dust temperature. G.-X. Li thanks Doug. N. C. Lin and Eugene Churazov for stimulating discussions. We thank our referee whose detailed comments help to improve our paper significantly.

REFERENCES

- Aguirre, J. E., Ginsburg, A. G., Dunham, M. K., et al. 2011, *ApJS*, 192, 4, doi: [10.1088/0067-0049/192/1/4](https://doi.org/10.1088/0067-0049/192/1/4)
- Ao, Y., Henkel, C., Menten, K. M., et al. 2013, *A&A*, 550, A135, doi: [10.1051/0004-6361/201220096](https://doi.org/10.1051/0004-6361/201220096)
- Bally, J., Stark, A. A., Wilson, R. W., & Henkel, C. 1987, *ApJS*, 65, 13, doi: [10.1086/191217](https://doi.org/10.1086/191217)
- Bally, J., Aguirre, J., Battersby, C., et al. 2010, *ApJ*, 721, 137, doi: [10.1088/0004-637X/721/1/137](https://doi.org/10.1088/0004-637X/721/1/137)
- Barnes, A. T., Longmore, S. N., Battersby, C., et al. 2017, *MNRAS*, 469, 2263, doi: [10.1093/mnras/stx941](https://doi.org/10.1093/mnras/stx941)
- Chen, B. Q., Li, G. X., Yuan, H. B., et al. 2020, *MNRAS*, 493, 351, doi: [10.1093/mnras/staa235](https://doi.org/10.1093/mnras/staa235)
- Churazov, E., Khabibullin, I., Sunyaev, R., & Ponti, G. 2017, *MNRAS*, 465, 45, doi: [10.1093/mnras/stw2750](https://doi.org/10.1093/mnras/stw2750)
- Csengeri, T., Urquhart, J. S., Schuller, F., et al. 2014, *A&A*, 565, A75, doi: [10.1051/0004-6361/201322434](https://doi.org/10.1051/0004-6361/201322434)
- Dahmen, G., Huttemeister, S., Wilson, T. L., & Mauersberger, R. 1998, *A&A*, 331, 959
- Dale, J. E., Kruijssen, J. M. D., & Longmore, S. N. 2019, *MNRAS*, 486, 3307, doi: [10.1093/mnras/stz888](https://doi.org/10.1093/mnras/stz888)
- Dobbs, C. L., Burkert, A., & Pringle, J. E. 2011, *MNRAS*, 413, 2935, doi: [10.1111/j.1365-2966.2011.18371.x](https://doi.org/10.1111/j.1365-2966.2011.18371.x)
- Emsellem, E., Renaud, F., Bournaud, F., et al. 2015, *MNRAS*, 446, 2468, doi: [10.1093/mnras/stu2209](https://doi.org/10.1093/mnras/stu2209)
- Federrath, C., Roman-Duval, J., Klessen, R. S., Schmidt, W., & Mac Low, M.-M. 2010, *A&A*, 512, A81, doi: [10.1051/0004-6361/200912437](https://doi.org/10.1051/0004-6361/200912437)
- Field, G. B., Goldsmith, D. W., & Habing, H. J. 1969, *ApJL*, 155, L149, doi: [10.1086/180324](https://doi.org/10.1086/180324)

- Fukui, Y., Ohama, A., Hanaoka, N., et al. 2014, *ApJ*, 780, 36, doi: [10.1088/0004-637X/780/1/36](https://doi.org/10.1088/0004-637X/780/1/36)
- Giannetti, A., Leurini, S., König, C., et al. 2017, *A&A*, 606, L12, doi: [10.1051/0004-6361/201731728](https://doi.org/10.1051/0004-6361/201731728)
- Ginsburg, A., Henkel, C., Ao, Y., et al. 2016, *A&A*, 586, A50, doi: [10.1051/0004-6361/201526100](https://doi.org/10.1051/0004-6361/201526100)
- Gong, Y., Fang, M., Mao, R., et al. 2017, *ApJL*, 835, L14, doi: [10.3847/2041-8213/835/1/L14](https://doi.org/10.3847/2041-8213/835/1/L14)
- Gravity Collaboration, Abuter, R., Amorim, A., et al. 2019, *A&A*, 625, L10, doi: [10.1051/0004-6361/201935656](https://doi.org/10.1051/0004-6361/201935656)
- Güsten, R., Nyman, L. Å., Schilke, P., et al. 2006, *A&A*, 454, L13, doi: [10.1051/0004-6361:20065420](https://doi.org/10.1051/0004-6361:20065420)
- Henshaw, J. D., Longmore, S. N., Kruijssen, J. M. D., et al. 2016, *MNRAS*, 457, 2675, doi: [10.1093/mnras/stw121](https://doi.org/10.1093/mnras/stw121)
- Heyer, M., & Dame, T. M. 2015, *ARA&A*, 53, 583, doi: [10.1146/annurev-astro-082214-122324](https://doi.org/10.1146/annurev-astro-082214-122324)
- Jefferson, S. M. R., Kruijssen, J. M. D., Krumholz, M. R., & Longmore, S. N. 2018, *MNRAS*, 478, 3380, doi: [10.1093/mnras/sty1154](https://doi.org/10.1093/mnras/sty1154)
- Jones, P. A., Burton, M. G., Cunningham, M. R., et al. 2008, *MNRAS*, 386, 117, doi: [10.1111/j.1365-2966.2008.13009.x](https://doi.org/10.1111/j.1365-2966.2008.13009.x)
- Kauffmann, J., Bertoldi, F., Bourke, T. L., Evans, II, N. J., & Lee, C. W. 2008, *A&A*, 487, 993, doi: [10.1051/0004-6361:200809481](https://doi.org/10.1051/0004-6361:200809481)
- Kauffmann, J., Pillai, T., Zhang, Q., et al. 2017a, *A&A*, 603, A89, doi: [10.1051/0004-6361/201628088](https://doi.org/10.1051/0004-6361/201628088)
- . 2017b, *A&A*, 603, A90, doi: [10.1051/0004-6361/201628089](https://doi.org/10.1051/0004-6361/201628089)
- Konstandin, L., Girichidis, P., Federrath, C., & Klessen, R. S. 2012, *ApJ*, 761, 149, doi: [10.1088/0004-637X/761/2/149](https://doi.org/10.1088/0004-637X/761/2/149)
- Kramer, C., Stutzki, J., Rohrig, R., & Corneliussen, U. 1998, *A&A*, 329, 249
- Kruijssen, J. M. D., Dale, J. E., & Longmore, S. N. 2015, *MNRAS*, 447, 1059, doi: [10.1093/mnras/stu2526](https://doi.org/10.1093/mnras/stu2526)
- Kruijssen, J. M. D., Longmore, S. N., Elmegreen, B. G., et al. 2014, *MNRAS*, 440, 3370, doi: [10.1093/mnras/stu494](https://doi.org/10.1093/mnras/stu494)
- Kruijssen, J. M. D., Dale, J. E., Longmore, S. N., et al. 2019, *MNRAS*, 484, 5734, doi: [10.1093/mnras/stz381](https://doi.org/10.1093/mnras/stz381)
- Krumholz, M. R., & Kruijssen, J. M. D. 2015, *MNRAS*, 453, 739, doi: [10.1093/mnras/stv1670](https://doi.org/10.1093/mnras/stv1670)
- Lada, C. J., Muench, A. A., Rathborne, J., Alves, J. F., & Lombardi, M. 2008, *ApJ*, 672, 410, doi: [10.1086/523837](https://doi.org/10.1086/523837)
- Launhardt, R., Zylka, R., & Mezger, P. G. 2002, *A&A*, 384, 112, doi: [10.1051/0004-6361:20020017](https://doi.org/10.1051/0004-6361:20020017)
- Li, G.-X. 2017a, *MNRAS*, 465, 667, doi: [10.1093/mnras/stw2707](https://doi.org/10.1093/mnras/stw2707)
- . 2017b, *MNRAS*, 471, 2002, doi: [10.1093/mnras/stx1622](https://doi.org/10.1093/mnras/stx1622)
- . 2018, *MNRAS*, 477, 4951, doi: [10.1093/mnras/sty657](https://doi.org/10.1093/mnras/sty657)
- Longmore, S. N., Bally, J., Testi, L., et al. 2013, *MNRAS*, 429, 987, doi: [10.1093/mnras/sts376](https://doi.org/10.1093/mnras/sts376)
- Mattern, M., Kauffmann, J., Csengeri, T., et al. 2018, *A&A*, 619, A166, doi: [10.1051/0004-6361/201833406](https://doi.org/10.1051/0004-6361/201833406)
- Molinari, S., Bally, J., Noriega-Crespo, A., et al. 2011, *ApJL*, 735, L33, doi: [10.1088/2041-8205/735/2/L33](https://doi.org/10.1088/2041-8205/735/2/L33)
- Molinari, S., Schisano, E., Elia, D., et al. 2016, *A&A*, 591, A149, doi: [10.1051/0004-6361/201526380](https://doi.org/10.1051/0004-6361/201526380)
- Muno, M. P., Baganoff, F. K., Bautz, M. W., et al. 2004, *ApJ*, 613, 326, doi: [10.1086/422865](https://doi.org/10.1086/422865)
- Nagai, M., Tanaka, K., Kamegai, K., & Oka, T. 2007, *PASJ*, 59, 25, doi: [10.1093/pasj/59.1.25](https://doi.org/10.1093/pasj/59.1.25)
- Nakashima, S., Koyama, K., Wang, Q. D., & Enokiya, R. 2019, *ApJ*, 875, 32, doi: [10.3847/1538-4357/ab0d82](https://doi.org/10.3847/1538-4357/ab0d82)
- Ossenkopf, V., & Henning, T. 1994, *A&A*, 291, 943
- Padoan, P., Jones, B. J. T., & Nordlund, Å. P. 1997, *ApJ*, 474, 730, doi: [10.1086/303482](https://doi.org/10.1086/303482)
- Pfalzner, S., Kirk, H., Sills, A., et al. 2016, *A&A*, 586, A68, doi: [10.1051/0004-6361/201527449](https://doi.org/10.1051/0004-6361/201527449)
- Ponti, G., Morris, M. R., Terrier, R., et al. 2015, *MNRAS*, 453, 172, doi: [10.1093/mnras/stv1331](https://doi.org/10.1093/mnras/stv1331)
- Ponti, G., Hofmann, F., Churazov, E., et al. 2019, *Nature*, 567, 347, doi: [10.1038/s41586-019-1009-6](https://doi.org/10.1038/s41586-019-1009-6)
- Roman-Duval, J., Jackson, J. M., Heyer, M., Rathborne, J., & Simon, R. 2010, *ApJ*, 723, 492, doi: [10.1088/0004-637X/723/1/492](https://doi.org/10.1088/0004-637X/723/1/492)
- Scalo, J., Vázquez-Semadeni, E., Chappell, D., & Passot, T. 1998, *ApJ*, 504, 835, doi: [10.1086/306099](https://doi.org/10.1086/306099)
- Schmiedeke, A., Schilke, P., Möller, T., et al. 2016, *A&A*, 588, A143, doi: [10.1051/0004-6361/201527311](https://doi.org/10.1051/0004-6361/201527311)
- Schuller, F., Menten, K. M., Contreras, Y., et al. 2009, *A&A*, 504, 415, doi: [10.1051/0004-6361/200811568](https://doi.org/10.1051/0004-6361/200811568)
- Shetty, R., Beaumont, C. N., Burton, M. G., Kelly, B. C., & Klessen, R. S. 2012, *MNRAS*, 425, 720, doi: [10.1111/j.1365-2966.2012.21588.x](https://doi.org/10.1111/j.1365-2966.2012.21588.x)
- Sofue, Y. 2013, *PASJ*, 65, 118, doi: [10.1093/pasj/65.6.118](https://doi.org/10.1093/pasj/65.6.118)
- Sormani, M. C., Treß, R. G., Ridley, M., et al. 2018, *MNRAS*, 475, 2383, doi: [10.1093/mnras/stx3258](https://doi.org/10.1093/mnras/stx3258)
- Spergel, D. N., & Blitz, L. 1992, *Nature*, 357, 665, doi: [10.1038/357665a0](https://doi.org/10.1038/357665a0)
- Spitzer, Jr., L., & Tomasko, M. G. 1968, *ApJ*, 152, 971, doi: [10.1086/149610](https://doi.org/10.1086/149610)
- Stutzki, J., & Guesten, R. 1990, *ApJ*, 356, 513, doi: [10.1086/168859](https://doi.org/10.1086/168859)
- Tasker, E. J., & Tan, J. C. 2009, *ApJ*, 700, 358, doi: [10.1088/0004-637X/700/1/358](https://doi.org/10.1088/0004-637X/700/1/358)
- Torii, K., Enokiya, R., Sano, H., et al. 2011, *ApJ*, 738, 46, doi: [10.1088/0004-637X/738/1/46](https://doi.org/10.1088/0004-637X/738/1/46)

- Tsuboi, M., Miyazaki, A., & Uehara, K. 2015, PASJ, 67, 90, doi: [10.1093/pasj/psv058](https://doi.org/10.1093/pasj/psv058)
- Urquhart, J. S., Thompson, M. A., Moore, T. J. T., et al. 2013, MNRAS, 435, 400, doi: [10.1093/mnras/stt1310](https://doi.org/10.1093/mnras/stt1310)
- Vazquez-Semadeni, E. 1994, ApJ, 423, 681, doi: [10.1086/173847](https://doi.org/10.1086/173847)
- Wang, K., Testi, L., Ginsburg, A., et al. 2015, MNRAS, 450, 4043, doi: [10.1093/mnras/stv735](https://doi.org/10.1093/mnras/stv735)
- Wolfire, M. G., McKee, C. F., Hollenbach, D., & Tielens, A. G. G. M. 2003, ApJ, 587, 278, doi: [10.1086/368016](https://doi.org/10.1086/368016)
- Wyrowski, F., Güsten, R., Menten, K. M., Wiesemeyer, H., & Klein, B. 2012, A&A, 542, L15, doi: [10.1051/0004-6361/201218927](https://doi.org/10.1051/0004-6361/201218927)
- Wyrowski, F., Güsten, R., Menten, K. M., et al. 2016, A&A, 585, A149, doi: [10.1051/0004-6361/201526361](https://doi.org/10.1051/0004-6361/201526361)
- Yamauchi, S., Kawada, M., Koyama, K., et al. 1990, ApJ, 365, 532, doi: [10.1086/169507](https://doi.org/10.1086/169507)
- Zhang, C.-P., Yuan, J.-H., Li, G.-X., Zhou, J.-J., & Wang, J.-J. 2017a, A&A, 598, A76, doi: [10.1051/0004-6361/201629771](https://doi.org/10.1051/0004-6361/201629771)
- Zhang, C.-P., Yuan, J.-H., Xu, J.-L., et al. 2017b, Research in Astronomy and Astrophysics, 17, 057, doi: [10.1088/1674-4527/17/6/57](https://doi.org/10.1088/1674-4527/17/6/57)
- Zhang, C.-P., Liu, T., Yuan, J., et al. 2018, ApJS, 236, 49, doi: [10.3847/1538-4365/aac513](https://doi.org/10.3847/1538-4365/aac513)
- Zhang, C.-P., Csengeri, T., Wyrowski, F., et al. 2019, A&A, 627, A85, doi: [10.1051/0004-6361/201834534](https://doi.org/10.1051/0004-6361/201834534)
- Zhou, C., Zhu, M., Yuan, J., et al. 2019, MNRAS, 485, 3334, doi: [10.1093/mnras/stz603](https://doi.org/10.1093/mnras/stz603)

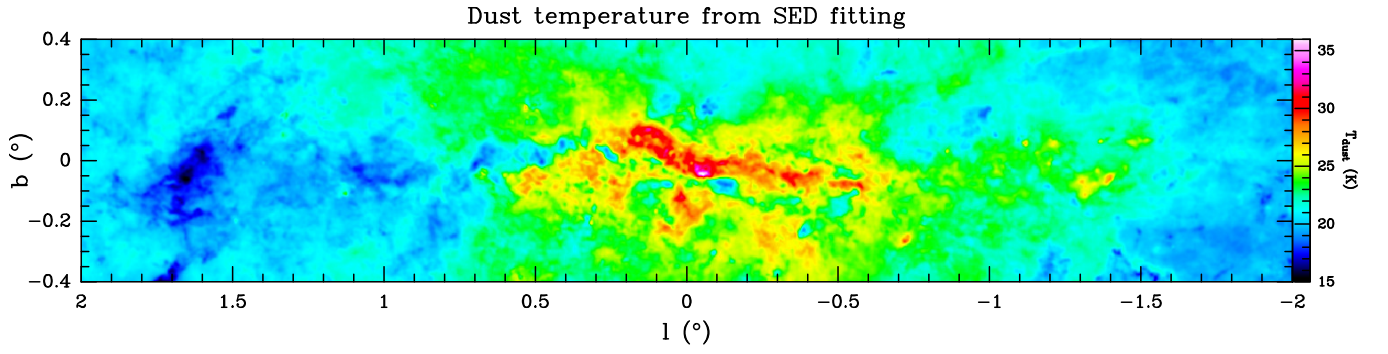


Figure 6. Dust temperature via fitting the SED of the multiwavelength observations on a pixel-by-pixel basis using the high-quality *Herschel* data whose wavelength ranges from 70 to 500 μm .

APPENDIX

A. TEMPERATURE MAP

In Figure 6 we present the map of dust temperature. See Section 2 for details.

Table 1. Parameters of identified Gaussian clumps.

Clumps No.	l, b ($^{\circ}, ^{\circ}$)	FWHM ($''$)	R_{eff} (pc)	T_{dust} (K)	$I_{870\mu\text{m}}$ (Jy beam $^{-1}$)	$S_{870\mu\text{m}}$ (Jy)	M_{H_2} ($10^3 M_{\odot}$)	N_{H_2} (10^{23}cm^{-2})	n_{H_2} (10^4cm^{-3})
1	(0.6765, -0.0268)	29.1	0.68	23.6 ± 2.4	139.82	331.45	92.2 ± 12.8	28.8 ± 4.0	51.9 ± 7.2
2	(0.6649, -0.0334)	34.1	0.80	24.3 ± 2.4	127.47	405.40	108.2 ± 14.9	24.5 ± 3.4	37.7 ± 5.2
3	(0.6545, -0.0406)	42.3	0.99	23.0 ± 2.3	46.17	266.50	76.7 ± 10.8	11.3 ± 1.6	14.0 ± 2.0
4	(0.6667, -0.0203)	42.0	0.98	21.2 ± 2.1	31.21	217.21	70.1 ± 10.1	10.5 ± 1.5	13.1 ± 1.9
5	(0.6923, -0.0268)	71.2	1.66	19.9 ± 2.0	21.92	325.98	115.1 ± 16.9	6.0 ± 0.9	4.4 ± 0.7
6	(0.6442, -0.0506)	51.6	1.20	20.7 ± 2.1	15.65	130.80	43.7 ± 6.3	4.3 ± 0.6	4.4 ± 0.6
7	(-0.1330, -0.0824)	58.9	1.37	18.7 ± 1.9	10.82	130.81	50.9 ± 7.7	3.9 ± 0.6	3.5 ± 0.5
8	(-0.3844, -0.2427)	32.5	0.76	21.9 ± 2.2	11.09	32.06	9.9 ± 1.4	2.5 ± 0.4	4.0 ± 0.6
9	(0.6750, -0.0056)	68.5	1.60	18.8 ± 1.9	10.59	141.75	54.7 ± 8.2	3.1 ± 0.5	2.4 ± 0.4
10	(0.6295, -0.0604)	69.9	1.63	19.9 ± 2.0	10.26	142.89	50.5 ± 7.4	2.7 ± 0.4	2.1 ± 0.3
11	(0.4769, -0.0058)	56.2	1.31	18.2 ± 1.8	9.39	85.24	34.5 ± 5.2	2.9 ± 0.4	2.7 ± 0.4
12	(0.6761, -0.0395)	27.5	0.64	25.1 ± 2.5	10.38	50.32	12.9 ± 1.8	4.5 ± 0.6	8.6 ± 1.2
13	(0.6536, -0.0148)	41.6	0.97	19.4 ± 1.9	8.48	56.04	20.7 ± 3.1	3.2 ± 0.5	4.0 ± 0.6
14	(-0.5590, -0.1044)	41.0	0.95	21.5 ± 2.2	8.01	40.18	12.7 ± 1.8	2.0 ± 0.3	2.6 ± 0.4
15	(-0.0571, -0.0455)	64.2	1.49	36.2 ± 3.6	7.86	94.26	14.9 ± 1.9	1.0 ± 0.1	0.8 ± 0.1
16	(-0.1062, -0.0703)	74.9	1.74	19.2 ± 1.9	7.74	125.70	47.1 ± 7.0	2.2 ± 0.3	1.6 ± 0.2
17	(0.2551, 0.0160)	70.6	1.64	19.7 ± 2.0	6.93	154.26	55.6 ± 8.2	2.9 ± 0.4	2.2 ± 0.3
18	(0.6621, -0.0449)	22.9	0.53	24.4 ± 2.4	7.29	11.45	3.0 ± 0.4	1.5 ± 0.2	3.5 ± 0.5
19	(-0.0233, -0.0699)	89.3	2.08	23.0 ± 2.3	6.32	179.16	51.5 ± 7.2	1.7 ± 0.2	1.0 ± 0.1
20	(0.3758, 0.0410)	31.3	0.73	22.7 ± 2.3	5.95	15.93	4.7 ± 0.7	1.3 ± 0.2	2.1 ± 0.3
21	(0.6816, -0.0179)	24.2	0.56	19.9 ± 2.0	8.17	15.91	5.6 ± 0.8	2.5 ± 0.4	5.5 ± 0.8
22	(1.1255, -0.1083)	38.9	0.91	24.0 ± 2.4	5.32	24.84	6.7 ± 0.9	1.2 ± 0.2	1.6 ± 0.2
23	(0.4934, 0.0179)	61.4	1.43	19.0 ± 1.9	5.19	59.99	22.7 ± 3.4	1.6 ± 0.2	1.4 ± 0.2
...									

Others are listed only in online table.

B. ESTIMATION OF CLUMP DENSITY

A crucial step in our analysis is to estimate the density of the clumps. Ideally, for a clump of a constant density, its density can be estimated using

$$\rho_0 = \frac{m_0}{4/3 \pi r_0^3} . \quad (\text{B1})$$

where r_0 is the clump radius and m_0 is the mass. However, in our analysis, due to the fact that we can only trace the distribution of gas in 2D, as well as our clump extraction procedure, both m_{clump} and r_{clump} might have some biases. To access these effects, we have performed a simulation where we created a clump of a constant density in 3D, projected it to 2D, and computed the mass and size of the simulated clump by recovering it using the **GAUSSCLUMPS** algorithm. Assuming that the original clump has a mass of $m_{3\text{D}}$ and size of $r_{3\text{D}}$, and the recovered clump has a mass of m_{clump} and a size of r_{clump} , we find

$$m_{\text{clump}} = 0.76 \times m_{3\text{D}} , \quad (\text{B2})$$

and

$$r_{\text{clump}} = 0.72 \times r_{3\text{D}} . \quad (\text{B3})$$

To accurately derive the clump density, we propose to use the equation

$$\rho_{\text{clump}} = 0.12 \times m_{\text{clump}} r_{\text{clump}}^{-3} , \quad (\text{B4})$$

such that $\rho_{3\text{D}} = \rho_{\text{clump}}$ is guaranteed.